AIAA JOURNAL
Vol. 34, No. 7, July 1996

Three-Dimensional Shock/Boundary-Layer Interaction Using Reynolds Stress Equation Turbulence Model

Ge-Cheng Zha* and Doyle Knight†
Rutgers University, Piscataway, New Jersey 08855-0909

The three-dimensional crossing shock wave/turbulent-boundary-layer interaction caused by an asymmetric 7 × 11-deg double fin with incoming Mach number 3.95 was simulated using the Reynolds-averaged Navier–Stokes equations with a full Reynolds stress equation turbulence model. An implicit approximate factorization method is used for the temporal integration. Roe's scheme is used for evaluation of the convective terms of the mean flow and Reynolds stress equations with a third-order MUSCL-type differencing. The computed surface pressure is in good agreement with the experiment. The computed heat transfer coefficient shows a modest improvement compared with previous results obtained using the k–ϵ model with Chien's low-Reynolds-number correction. Both computations of the heat transfer display significant deviations from experiment. Tests of the grid refinement, different upstream boundary-layer profiles, and different isothermal wall temperature also are presented.

I. Introduction

WITH the development of aerospace technology, the supersonic and hypersonic aerodynamic design for aircraft attracts more attention. Even though the Concorde supersonic transport and the Space Shuttle have been in use for more than a decade, many supersonic aerodynamic problems are not well understood. An important problem is the shock wave/turbulent-boundary-layer interaction, which enhances the heat transfer and the skin friction and reduces the kinetic energy of the flow. Good understanding and prediction of the shock wave/turbulent-boundary-layer interaction will provide important information to aircraft designers. Knight[1] recently reviewed the status of the computational fluid dynamics research on three-dimensional shock wave/turbulent-boundary-layer interaction for a family of geometries. It is now generally agreed that the wave structure and pressure field can be accurately predicted in general for simple three-dimensional shock wave/turbulent-boundary-layer interactions, e.g., sharp fin and swept compression corner. However, the predicted heat transfer typically shows a large deviation from experiment. Such disagreement is apparently attributable to the inadequacy of the eddy viscosity concept inherent in algebraic and k–ϵ models. Reynolds stress equation (RSE) turbulence models are promising candidates because they naturally incorporate the nonlocal and history effects of the Reynolds stress development. However, RSE models have been applied mainly to incompressible flows, but they recently have begun to be used also for compressible flows.[2–6] However, most of the work is limited to two-dimensional compressible flows, and no work has been done to apply an RSE model to a three-dimensional shock wave/turbulent-boundary-layer interaction.

Because the structure of shock wave/turbulent-boundary-layer interactions for simple geometries is generally well understood, attention has focused in recent years on more complex three-dimensional shock wave/turbulent-boundary-layer interaction, including the crossing-shock (double fin) interaction (Fig. 1). This configuration has been proposed as a possible hypersonic inlet.[7,8] Virtually all research to date has focused on the symmetric crossing-shock interaction.[9–16] Collaborative experimental and computational research has elucidated the wave and streamline structure. Good agreement has been observed between computed and experimental surface pressure and flowfield profiles; however, computed heat transfer typically overestimates the experimental data.[1,10,17] Various modifications to two equation turbulence models have been tested to improve the prediction of heat transfer.[16]

There are only a few studies of the asymmetric crossing-shock interaction. Garrison[18] obtained surface flow visualization and planar laser-sheet images for a series of crossing-shock configurations at Mach 3.9. Zheltovodov et al.[19] obtained surface pressure, heat transfer, and flow visualization for several asymmetric crossing-shock interactions at Mach 3 and 4. Knight et al.[20] computed two crossing-shock interactions at Mach 4 corresponding to experimental configurations of Garrison[18] and Zheltovodov et al.,[19] using Chien's k–ϵ model.[40] Good agreement was observed between computed and experimental surface pressure and flow visualization; however, surface heat transfer was overpredicted by 100% within the three-dimensional interaction region.

The purpose of this paper is to study the asymmetric three-dimensional crossing shock wave/turbulent-boundary-layer interaction with a full RSE model of turbulence. The objectives are twofold. First, we seek to evaluate the accuracy of a full RSE model by comparison with the experimental data of Zheltovodov et al.[19] for a Mach 3.95 asymmetric 7 × 11-deg crossing shock. The previous results of Knight et al.[20] using Chien's k–ϵ model also are presented for comparison with the full RSE model. Second, we examine the flowfield structure predicted by the RSE model, and offer some conjectures regarding the enhancement of turbulence by the shock wave/boundary-layer interaction.

II. Governing Equations and Turbulence Modeling

The governing equations are the Reynolds-averaged Navier–Stokes equations with the additional equations for the Reynolds stresses, the turbulent dissipation rate, and heat flux terms. The

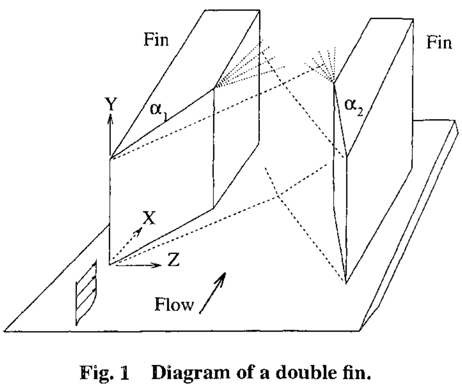

Fig. 1 Diagram of a double fin.

Received Oct. 9, 1995; revision received Feb. 23, 1996; accepted for publication Feb. 23, 1996. Copyright © 1996 by Ge-Cheng Zha and Doyle Knight. Published by the American Institute of Aeronautics and Astronautics, Inc., with permission.

*Postdoctoral Research Associate, Department of Mechanical and Aerospace Engineering, P.O. Box 909. Member AIAA.

†Professor, Department of Mechanical and Aerospace Engineering, P.O. Box 909. Associate Fellow AIAA.

Reynolds-averaged Navier–Stokes equations for conservation of mass, momentum, and energy are

$$\partial_t\bar{\rho} + \partial_k\bar{\rho}\tilde{u}_k = 0 \tag{1}$$

$$\partial_t\bar{\rho}\tilde{u}_i + \partial_k\bar{\rho}\tilde{u}_i\tilde{u}_k = -\partial_i\bar{p} + \partial_k(-\overline{\rho u_i''u_k''} + \bar{\tau}_{ik}) \tag{2}$$

$$\begin{aligned}\partial_t\bar{\rho}\tilde{e} + \partial_k(\bar{\rho}\tilde{e} + \bar{p})\tilde{u}_k &= \partial_k(-c_p\overline{\rho T''u_k''} - \bar{q}_k)\\ &+ \partial_k(-\overline{\rho u_i''u_k''}\tilde{u}_i + \tilde{u}_i\bar{\tau}_{ik}) + \partial_k\left(-\tfrac{1}{2}\overline{\rho u_j''u_j''u_k''} + \overline{u_i''\tau_{ik}}\right)\end{aligned} \tag{3}$$

where $\partial_t = \partial/\partial t$, $\partial_k = \partial/\partial x_k$ and the Einstein summation convention is employed. The overbar denotes a conventional Reynolds average, and the tilde is used to denote the Favre mass average. A double prime ($''$) represents fluctuations with respect to the Favre average, whereas a single prime ($'$) stands for fluctuations with respect to the Reynolds average.

In the above equations, $\bar{\rho}$ is the mean density, $\tilde{u}_i$ is the mass-averaged Cartesian velocity with $(\tilde{u}_1, \tilde{u}_2, \tilde{u}_3) = (\tilde{u}, \tilde{v}, \tilde{w})$, $\bar{p}$ is the mean pressure, and $\tilde{e}$ is the mass-averaged total energy per unit mass. The following relations are employed to evaluate $\bar{p}$ and $\tilde{e}$:

$$\bar{p} = \bar{\rho}R\tilde{T} \tag{4}$$

$$\tilde{e} = c_v\tilde{T} + \tfrac{1}{2}\tilde{u}_i\tilde{u}_i + k \tag{5}$$

where k is the mass-averaged turbulence kinetic energy

$$\bar{\rho}k = \tfrac{1}{2}\overline{\rho u_i''u_i''} \tag{6}$$

The mean molecular viscous stress $\bar{\tau}_{ij}$ is

$$\bar{\tau}_{ij} = -\tfrac{2}{3}\tilde{\mu}\partial_k\tilde{u}_k\delta_{ij} + \tilde{\mu}(\partial_i\tilde{u}_j + \partial_j\tilde{u}_i) \tag{7}$$

where $\tilde{\mu} \equiv \mu(\tilde{T})$ is determined by the Sutherland law. Similarly, the molecular heat flux is

$$\bar{q}_k = -\frac{c_p\tilde{\mu}}{Pr}\partial_k\tilde{T} \tag{8}$$

where Pr is the molecular Prandtl number.

In the energy equation, the triple velocity correlation $\frac{1}{2}\overline{\rho u_j''u_j''u_k''}$ and the velocity–molecular shear correlation $\overline{u_i''\tau_{ik}}$ are considered small and are neglected.[1]

To close the above equations, a turbulence model needs to be introduced to determine the Reynolds stress $-\overline{\rho u_i''u_j''}$ and the turbulent heat flux $-c_p\overline{\rho T''u_i''}$. A full RSE turbulence model developed by Gnedin and Knight[21] is employed. The model is an extension of an incompressible-flow RSE model to its compressible counterpart with some modification regarding the compressibility effects. The model is presented below.

The equation for the Reynolds stress is

$$\partial_t\overline{\rho u_i''u_j''} + \partial_k\overline{\rho u_i''u_j''}\,\tilde{u}_k = A_{ij} + B_{ij} + C_{ij} + D_{ij} \tag{9}$$

where the A_{ij}, B_{ij}, C_{ij}, and D_{ij} are the Reynolds stress production term, diffusion term, pressure–rate of strain correlation, and dissipation term. They are expressed as

$$A_{ij} = -\overline{\rho u_j''u_k''}\partial_k\tilde{u}_i - \overline{\rho u_i''u_k''}\partial_k\tilde{u}_j \tag{10}$$

$$B_{ij} = \partial_k\{-\overline{\rho u_i''u_j''u_k''} + \overline{u_j''\tau_{ik}} + \overline{u_i''\tau_{jk}} - \overline{pu_i''}\delta_{jk} - \overline{pu_j''}\delta_{ik}\} \tag{11}$$

$$C_{ij} = \overline{p(\partial_j u_i'' + \partial_i u_j'')} \tag{12}$$

$$D_{ij} = -\overline{\tau_{ik}\partial_k u_j''} - \overline{\tau_{jk}\partial_k u_i''} \tag{13}$$

The production term of the Reynolds stress requires no further modeling because the Reynolds stress and mean velocity are dependent variables.

In the RSE model, the diffusion term is modeled as

$$\begin{aligned}B_{ij} = \partial_k\big\{&C_{d_1}(k/\bar{\rho}\epsilon)[\overline{\rho u_i''u_m''}\partial_m(\overline{\rho u_j''u_k''})\\ &+ \overline{\rho u_j''u_m''}\partial_m(\overline{\rho u_i''u_k''}) + \overline{\rho u_k''u_m''}\partial_m(\overline{\rho u_i''u_j''})]\big\}\\ &+ \partial_k\{\tilde{\nu}[\partial_k(\overline{\rho u_i''u_j''}) + \partial_j(\overline{\rho u_i''u_k''}) + \partial_i(\overline{\rho u_j''u_k''})]\}\end{aligned} \tag{14}$$

where $\tilde{\nu} \equiv \tilde{\mu}/\bar{\rho}$ and C_{d_1} is a constant. This model is an extension of the incompressible-flow model of Launder et al.[22]

The correlation of the instantaneous pressure and fluctuating rate of strain is modeled as

$$C_{ij} = -C_{p_1}(\epsilon/k)\left\{\overline{\rho u_i''u_j''} - \tfrac{2}{3}\bar{\rho}k\delta_{ij}\right\} + C_{p_2}\bar{\rho}k\{\partial_j\tilde{u}_i + \partial_i\tilde{u}_j\} \tag{15}$$

where C_{p_1} and C_{p_2} are constants. This is an extension of Rotta's model[23] for incompressible flow.

An isotropic dissipation model with compressibility effect is used to determine the dissipation term

$$D_{ij} = -\tfrac{2}{3}\bar{\rho}\epsilon\delta_{ij} \tag{16}$$

According to Sarkar et al.[24] and Zeman,[25]

$$\bar{\rho}\epsilon = \bar{\rho}\,(\epsilon_s + \epsilon_c)$$

where $\epsilon_c = C_k\epsilon_s M_t^2$ and the turbulence Mach number is $M_t = \surd(2k)/\tilde{a}$. Even though this compressible-flow effect for dissipation is incorporated in the computer code, it is actually not used, and $C_k = 0$ because, for wall-bounded flows, this effect is small and the above modification is also questionable.[26]

The conventional equation[27] is employed for ϵ_s:

$$\begin{aligned}\partial_t\bar{\rho}\epsilon_s + \partial_k\bar{\rho}\epsilon_s\tilde{u}_k &= -C_{\epsilon_1}(\epsilon_s/k)\overline{\rho u_i''u_k''}\partial_k\tilde{u}_i\\ &- C_{\epsilon_2}\bar{\rho}\left(\epsilon_s^2/k\right) + \partial_k\left[\left(C_{\epsilon_3}\bar{\rho}(k^2/\epsilon) + \tilde{\mu}\right)\partial_k\epsilon_s\right]\end{aligned} \tag{17}$$

where C_{ϵ_1}, C_{ϵ_2}, and C_{ϵ_3} are constants.

The turbulent heat flux is modeled using a gradient diffusion hypothesis,

$$-c_p\overline{\rho T''u_i''} = c_p\bar{\rho}C_h(k^2/\epsilon)\partial_i\tilde{T} \tag{18}$$

where C_h is a constant.

Table 1 presents the values of the closure constants of the present RSE turbulence model.[21]

There are two ways to treat the flowfield in the vicinity of the walls: one is to use wall functions and the other is to use the low-Reynolds-number correction to resolve the viscous sublayer. The wall-function method is chosen in this paper to save computation time. The asymptotic solutions of the above governing equations in the fully turbulent region of a two-dimensional boundary layer were obtained previously.[28] The asymptotic solutions (wall functions) are

$$\begin{aligned}\frac{\tilde{u}}{u_\infty} - \frac{1}{2A^2}\Bigg\{B + \sqrt{B^2 + 4A^2}\sin\Bigg[A\frac{\bar{u}_*}{u_\infty\kappa}(\log y^+ + B'\kappa)\\ - \arcsin\left(\frac{B}{\sqrt{B^2 + 4A^2}}\right)\Bigg]\Bigg\} = 0\end{aligned} \tag{19}$$

Table 1 Turbulence model constants

Quantity	Value
C_{d_1}	0.086
C_{p_1}	4.325
C_{p_2}	0.179
C_{ϵ_1}	1.01
C_{ϵ_2}	1.80
C_{ϵ_3}	0.10
C_k	0.0
C_h	0.0857

where

$$y^+ = \frac{y\bar{u}_*\bar{\rho}_w}{\tilde{\mu}_w}$$

$$A^2 = \frac{Pr_t(\gamma - 1)}{2}M_\infty^2\frac{T_\infty}{\tilde{T}_w}$$

$$B = -Pr_t\frac{\bar{q}_w U_\infty}{c_p\bar{\tau}_w\tilde{T}_w}$$

$$B' = 5.0$$

$$\kappa = 0.41$$

$$(\bar{\rho}_w/\bar{\rho}) - 1 - B(\tilde{u}/u_\infty) + A^2(\tilde{u}/u_\infty)^2 = 0 \tag{20}$$

$$\bar{p} = \bar{R}\bar{\rho}_w\tilde{T}_w \tag{21}$$

$$k_{\text{iso}}(\tilde{T}_w - \tilde{T}_{\text{wall}}) + (1 - k_{\text{iso}})\,(\bar{q}_w - \bar{q}_{\text{wall}}) = 0 \tag{22}$$

$$\epsilon - \frac{\alpha_4\bar{u}_*^3}{y}\left(\frac{\bar{\rho}_w}{\bar{\rho}}\right)^{1.5} = 0 \tag{23}$$

$$\overline{\rho u''u''} - \alpha_1\bar{\tau}_w = 0 \tag{24}$$

$$\overline{\rho v''v''} - \alpha_2\bar{\tau}_w = 0 \tag{25}$$

$$\overline{\rho w''w''} - \alpha_3\bar{\tau}_w = 0 \tag{26}$$

$$\overline{\rho u''v''} + \bar{\tau}_w = 0 \tag{27}$$

$$\tilde{v} = \tilde{w} = 0 \tag{28}$$

where $Pr_t = 0.9$; u_∞ and T_∞ are reference velocity and temperature, respectively; $k_{\text{iso}} = 1$ indicates a specified wall temperature; and $k_{\text{iso}} = 0$ implies a specified wall heat flux. The constants α_1, α_2, α_3, and α_4 are defined as

$$\alpha_1 = (C_{p_1} + 2)\sqrt{\frac{2}{3(C_{p_1} - 1 - 1.5C_{p_1}C_{p_2})}} \tag{29}$$

$$\alpha_2 = \frac{C_{p_1} - 1}{C_{p_1} + 2}\alpha_1 \tag{30}$$

$$\alpha_3 = \alpha_2 \tag{31}$$

$$\alpha_4^2 = \frac{C_{\epsilon_3}\alpha^2}{(C_{\epsilon_2}/\alpha) - [C_{\epsilon_1}C_{p_1}/(\alpha_2 - C_{p_2}\alpha)\alpha^2]} \tag{32}$$

where $\alpha = \frac{1}{2}(\alpha_1 + \alpha_2 + \alpha_3)$.

These wall functions are extended in a straightforward manner to three-dimensional flow under the assumption that the turbulent shear stress is locally aligned with the direction of the mean flow velocity at the point of application of the wall functions. The pressure-gradient correction[29] to the wall functions is omitted. The relative contribution of the pressure-gradient terms to the Reynolds shear stress at the point of application of the wall functions[29] is proportional to y and thus decreases with decreasing y. As indicated in Sec. IV.B, the computed flowfield is insensitive to the y value of the point of application of the wall functions, and thus it is concluded that the pressure-gradient correction to the wall functions would have a small effect on the computed flowfield.

III. Numerical Algorithm

An implicit finite volume approximate factorization method is used to solve the discretized equations. The individual block matrix size is 12 × 12 because the equations are fully coupled. The modified approximate factorization method of Vandromme is employed[4,5]:

$$\{I - \Delta tS\}\left\{I + \frac{\Delta t}{V}\frac{\partial C}{\partial \zeta}\right\}\left\{I + \frac{\Delta t}{V}\frac{\partial B}{\partial \eta}\right\} \times \left\{I + \frac{\Delta t}{V}\frac{\partial A}{\partial \xi}\right\}\Delta Q^{n+1} = \text{RHS}^n \tag{33}$$

For the source-term Jacobian, we only keep the diagonal elements of the original source-term Jacobian. This treatment enhances diagonal dominance.

Roe's flux difference splitting scheme is employed for the mean flow and RSE convective terms because of its ability to obtain high-resolution shock waves and low numerical diffusion for viscous flows. The third-order MUSCL-type differencing is used for these convective terms.[30] However, because central differencing is used for the viscous and turbulence diffusion and the source terms, the general accuracy of the solution is second order. The temporal discretization is first order to save CPU time because only the steady-state solutions are of interest. First-order accuracy is used also for the left-hand-side implicit operators to save CPU time and to obtain diagonal dominance.

At the turbulent–nonturbulent interface, the turbulence variables have discontinuous derivatives, as observed by other researchers.[29,31] The flux limiters, designed to achieve monotone shock-wave profiles for the higher-order upwind schemes, are essential to capture the turbulent–nonturbulent interface and make the computation stable even when there is no shock wave in the flowfield. Two smooth limiters, Roe's Super Bee limiter and Minmod limiter, were tested with the MUSCL-type reconstruction.[30,32,33] The numerical tests indicated that the Minmod limiter was able to reduce the residual to machine zero, whereas the Super Bee limiter was only able to reduce the residual by one order of magnitude. Using the Minmod limiter in the present computations, the variable profiles captured at the turbulent–nonturbulent interface are as sharp as those resolved by the boundary-layer code computation, which used a much finer adaptive mesh.[34]

IV. Results and Discussion

To ensure the accuracy of the three-dimensional computer code, several validation computations were performed. Computed supersonic laminar flat-plate results have no distinguishable difference from the analytical Blasius solution.[35] This ensures that the code has small numerical dissipation. For the supersonic turbulent flat-plate flow, excellent agreement was also obtained by comparing the results with those from a separate computation of the compressible boundary-layer equations with the same RSE model.[34] This ensures that the turbulence model is correctly implemented.

The asymmetric double-fin channel was calculated using the aforementioned algorithm. The two fins have angles of 7 and 11 deg. The Mach number of the upstream flow is 3.95. The thin boundary layers on the fin surfaces were not resolved, and slip boundary conditions were applied at the fin surfaces. Previous studies of the single-fin interactions[36] demonstrate that the bottom-wall shock wave/turbulent-boundary-layer interaction is essentially unaffected by the boundary layer on the fin. Of course, sufficiently far downstream of the intersection of the crossing shocks, the shocks will interact with the turbulent boundary layers on the sidewall fin surfaces. However, in the present study, nearly all experimental data are obtained upstream of the sidewall shock wave/turbulent-boundary-layer interactions, and consequently, the omission of the fin boundary layers does not affect comparison with the experiment in this regard. Also, Bardina and Coakley[17] observed that the treatment of the fin boundary layers as laminar–turbulent affected the flowfield in the immediate vicinity of the fin–plate junction for a Mach 8.3 crossing-shock interaction. However, in the present study, experimental data are available only in the central portion of the flow, and thus our comparison with experiment is expected to be unaffected by the use of slip boundary conditions on the fins.

A boundary-layer equation code with the same RSE turbulence model[21] was used to generate the upstream variable profiles. The upstream boundary-layer profiles agree reasonably well with the

Table 2 Flow conditions

Parameter	Experiment	Computation
M_∞	3.95	3.95
$Re_{\delta\infty}$	3.033×10^5	3.033×10^5
$\delta^*_\infty(m)$	1.12×10^{-3}	1.12×10^{-3}
$\theta_\infty(m)$	1.3×10^{-4}	1.246×10^{-4}
$C_{h\infty}$	7.9×10^{-4}	5.91×10^{-4}
$P_{t\infty}$(MPa)	1.492	1.492
$T_{t\infty}$ K	260.4	260.4

Table 3 Grid sizes

Parameter	Baseline case	Refined in		
		x	y	z
N_x	101	201	101	101
N_y	69	69	137	69
N_z	49	49	49	97
y_1^+	29	29	20.9	29
Δy_1^+	6.21	6.21	2.64	6.21
y_1/δ_∞	0.0326	0.0326	0.02374	0.0326
$y_{\max}/\delta_\infty$	15.51	15.51	15.51	15.51
$\Delta y_{\min}/\delta_\infty$	0.007	0.007	0.003	0.007
$\Delta y_{\max}/\delta_\infty$	1.16	1.16	0.621	1.16
$\Delta x/\delta_\infty$	0.5	0.25	0.5	0.5
$\Delta z_{\min}/\delta_\infty$	0.2	0.2	0.2	0.1
$\Delta z_{\max}/\delta_\infty$	0.4762	0.4762	0.4762	0.2881

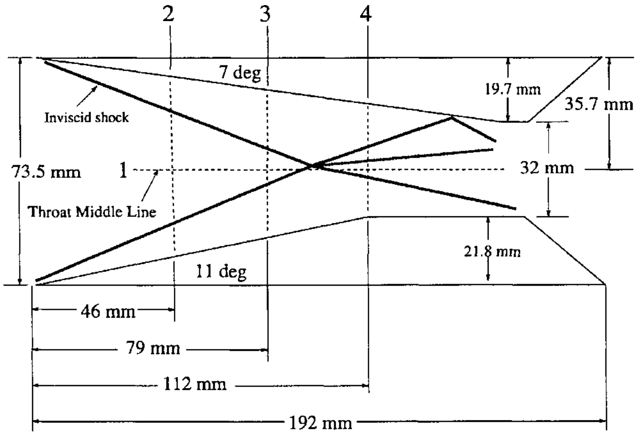

Fig. 2 7 × 11-deg double-fin measurement locations 1, 2, 3, and 4.

law of the wall and wake.[21,37] The upstream turbulent variable profiles determined by the present model also agree favorably with the available experimental data[38] at Mach 3. Because it generally is not possible for the computed upstream profiles to exactly match all of the experimental parameters upstream of the intersection, the highest priority was matching the experimental displacement thickness, which is considered to have the best measurement accuracy. A computational test is conducted to study the influence of the variation of upstream profiles and the results are given in Sec. IV.B. Table 2 presents the flow parameters for the computations.

A. Baseline Case

As the baseline case, the first computation for this asymmetric double-fin flow used a mesh size equal to 101 × 69 × 49 in the x, y, and z directions. The y^+ of the first grid point adjacent to the wall is equal to 28.96 at the inflow boundary. A series of computations was carried out to test the dependence of the present RSE model on the grid refinement, upstream profiles, and wall temperature. Those results are compared with this baseline case in Sec. IV.B. Table 3 provides the mesh-size information for the baseline case and grid refinement cases.

Figure 2 shows the experimental measurement locations on the bottom surface of the channel. Location 1 is the throat middle line, which is along the streamwise direction. Locations 2, 3, and 4 are in the spanwise direction with the streamwise positions equal to 46, 79, and 112 mm, respectively. Figures 3 and 4 are the pressure distributions compared with the experiment[20] and the results using Chien's k–ϵ model[20] at those locations. The experimental uncertainty in pressure measurement is ±0.5%. In Fig. 3, the computed pressures using both the RSE and k–ϵ model along the throat middle line agree well with the experiment except at the very end where there is a strong shock-wave reflection from the side walls. Because the side wall is treated as inviscid, the computed reflected sidewall shock is displaced downstream of the experimental shock. This is the cause of the deviation between computed and experimental pressures for $x > 140$ mm. The sections at $x = 46$ and 79 mm are located upstream of the inviscid intersection of the initial waves. The computed pressures agree closely with the experiment, as shown in Fig. 4. At $x = 112$ mm, which is located after the shock-wave intersection, there is a pressure plateau in the experiment that is not accurately represented in the present computation (see Fig. 4). The interaction of the shock waves with the turbulent boundary layer generates two counterrotating vortices. The computed-pressure valley at $x = 112$ mm corresponds to the vortex generated by the 11-deg fin. At the vortex-pressure valley region, the k–ϵ model predicted the pressure a little better than the RSE model. The disagreement between computed and experimental pressures at $x = 112$ mm may be attributable to differences in the strength of the vortex generated by the 11-deg fin; however, measurements of the vortex strength are unavailable. The computed and experimental results show that the sharp pressure gradient generated by the shock waves in the inviscid flowfield are greatly eased through the shock wave/turbulent boundary-layer interaction.

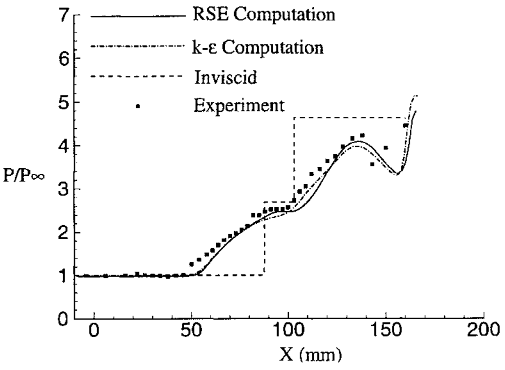

Fig. 3 Pressure distribution along the throat middle line.

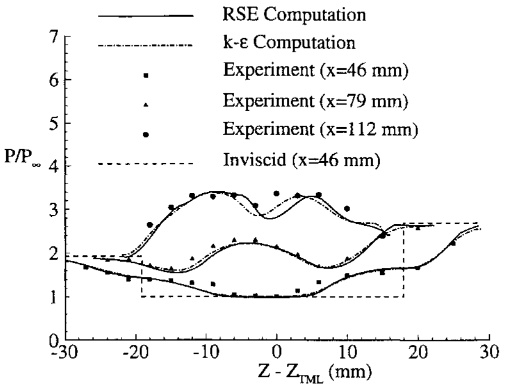

Fig. 4 Bottom-wall pressure distribution at $x = 46, 79$, and 112 mm.

Although there are no turbulence measurements for this configuration, it is nonetheless useful to examine the predictions of the RSE model for the turbulence kinetic energy. Figure 5 shows the mean streamline structure together with contours of the turbulence kinetic energy normalized by u^2_∞. The streamlines start at the channel entrance within the incoming boundary layer with the height equal to $0.1\delta_\infty$, where δ_∞ is the incoming boundary-layer thickness. At $x = 39.4$ mm, the individual counterrotating vortices, generated by

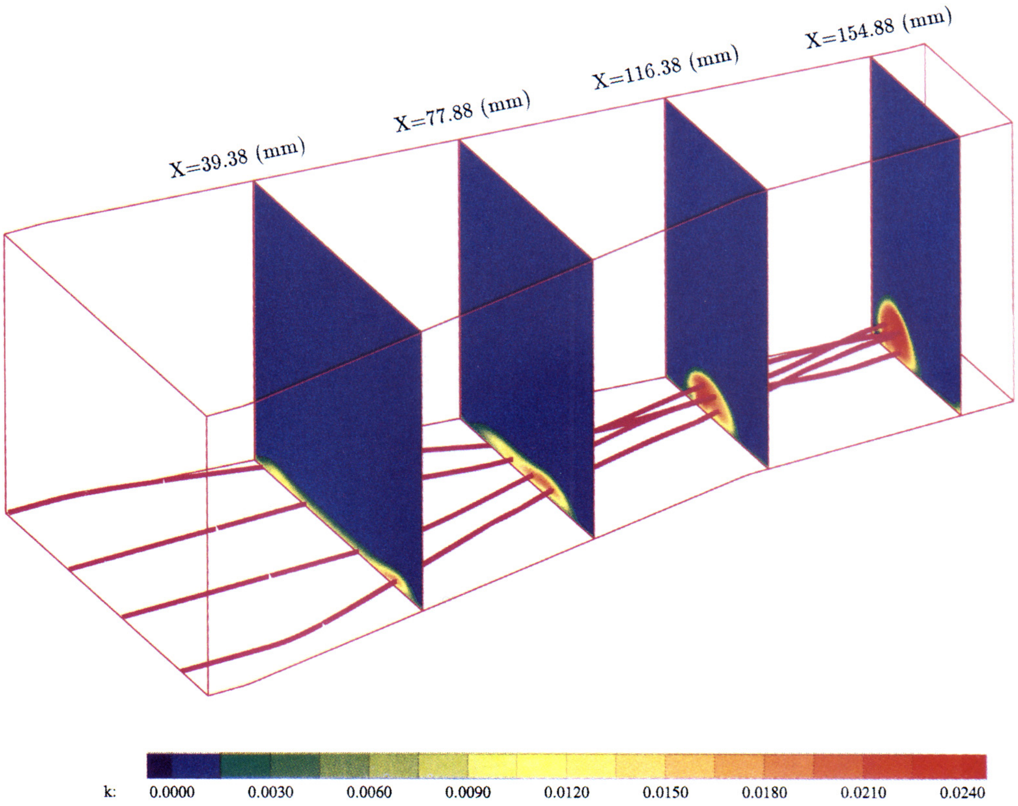

Fig. 5 Turbulent kinetic energy contours with streamlines at different locations.

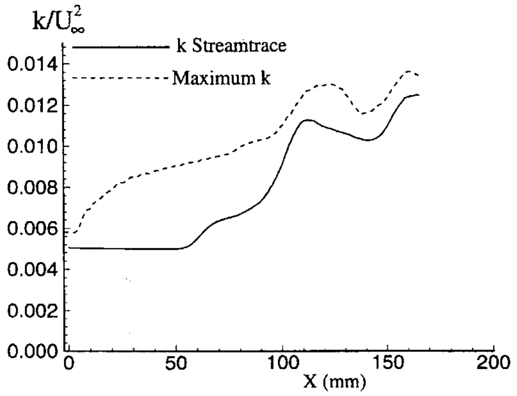

Fig. 6 Streamwise turbulent kinetic energy distributions.

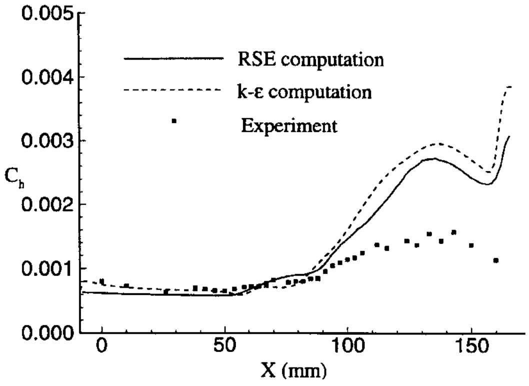

Fig. 7 Heat transfer coefficient distribution along the throat middle line.

the interaction of the fin-generated shock waves with the boundary layer, appear as enlarged elliptical regions. The high turbulent kinetic energy fluid in the lower portion of the incoming boundary layer is entrained into the vortex core, as indicated at $x = 77.9$ mm. At $x = 116.4$ mm, the vortices have combined to form a counter-rotating vortex pair, with maximum turbulence kinetic energy in the region between the two vortices.[39]

Figure 6 demonstrates the streamwise distribution of maximum turbulent kinetic energy and the turbulent kinetic energy distribution along a streamline. The starting point of the streamline is between the two middle streamlines in Fig. 5 and is located at $x = 0.0$ mm, $y = 0.1\delta_\infty$, and $z - z_{\mathrm{TML}} = -0.7$ mm. The starting point also has the same spanwise location as that of the inviscid shock intersection, which is close to the throat middle line (see Fig. 2). Along the streamline, it can be seen that the turbulent kinetic energy starts to increase at the location where the pressure starts to rise (see Fig. 3) before the inviscid shock intersection ($x = 91$ mm). It is attributable to the λ shock generated by the fin shock/boundary-layer interaction. The turbulence has a strong response because of the intersection of the shock waves with a enhancement of the turbulence kinetic energy from $x = 91$ to 110 mm. The turbulent kinetic energy reaches the peak at the location where the pressure has a plateau along the throat middle line. The turbulent kinetic energy decays after the peak whereas the pressure continues to rise downstream of the intersection of the inviscid shocks. The turbulence is enhanced again near the exit by the sidewall shock-wave reflection. The maximum turbulent kinetic energy distribution has a trend similar to that of the k distribution along the streamline. The maximum turbulent kinetic energy starts to rise at the entrance of the channel because the fin shock wave/turbulent-boundary-layer interactions start there. The shock wave/turbulent-boundary-layer interaction enhances the computed turbulence intensity by increasing the maximum value of k about 2.3 times from the channel entrance to the exit.

Figures 7 and 8 are the computed heat transfer coefficients compared with the experimental results and the computational results using Chien's k–ϵ model. The heat transfer coefficient C_h is defined as[20]

$$C_h \equiv \frac{q_w(x, z)}{\rho_\infty U_\infty c_p[T_w(x, z) - T_{aw}(x, z)]}$$

where $q_w(x, z) \equiv -\kappa_w \partial T/\partial y$ is the wall heat flux. The experimental uncertainty in C_h is ±10–15%. Two computations are needed

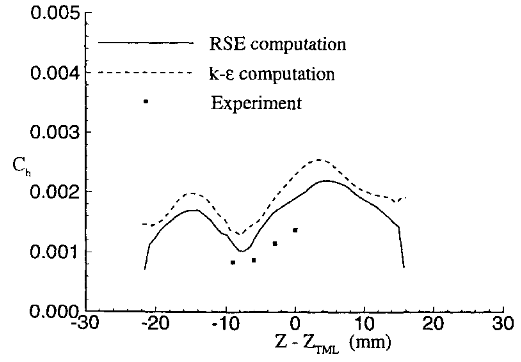

Fig. 8 Heat transfer coefficient distribution at the cross section x = 112 mm.

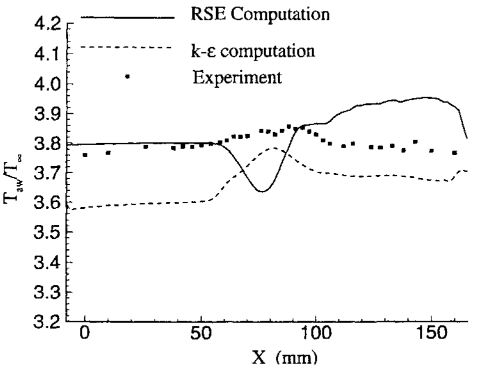

Fig. 9 Adiabatic wall-temperature distribution along the throat middle line.

to determine C_h, i.e., an isothermal case and an adiabatic case. For the isothermal case, the wall temperature is set to 265 K and the local heat transfer $q_w(x, z)$ is computed. For the adiabatic case, the zero wall-temperature gradient $\partial T/\partial y = 0$ is used as the boundary condition, and the local adiabatic wall temperature $T_{aw}(x, z)$ is computed.

The C_h measurement locations are the same as those for the pressure. Results at two representative locations are presented. Along the throat middle line shown in Fig. 7, the computational results using the k–ϵ model and the RSE model agree quite well with the experiment before the intersection of the shock waves. Both computational results are substantially higher than the experiment after the intersection of the shock wave interacting with the turbulent boundary layer. The maximum deviation of the RSE model from the experiment is 80% and the k–ϵ model is 100% at x = 138 mm. Figure 8 shows the heat transfer coefficient at the location x = 112 mm, which is downstream of the intersection of the inviscid shock waves. The heat transfer coefficient computed by the RSE model is lower than that computed by the k–ϵ model and is closer to the experiment. The RSE model overpredicted C_h by as much as 39%, but this still yielded a 28% improvement over the k–ϵ model. On the basis of these results, we conclude that the RSE turbulence model improves the prediction of the heat transfer for the intersecting shock waves/turbulent-boundary-layer interaction. However, the deviation from the experiment remains significant.

Figure 9 is the adiabatic wall temperature along the throat middle line. Both the RSE model and k–ϵ model predict the adiabatic wall temperature to within 5%. The experimental measurement uncertainty of the adiabatic wall temperature is ±0.3 K. Before the shock-wave intersection, the RSE model predicts an adiabatic wall temperature that is in closer agreement with the experiment. In the region of the shock wave/turbulent-boundary-layer interaction, the RSE model predicts an adiabatic wall-temperature variation that is opposite to the one obtained by the k–ϵ model.

The CPU time per time step for the baseline case is 113.8 s using the Cray C-90 with a single processor. Approximately 2000 time steps are needed to achieve a converged solution.[39]

B. Solution Convergence Tests

A series of computations is conducted to investigate the solution convergence of the baseline case. There are five tests, including grid refinement tests, the different isothermal wall temperature test, and the different upstream boundary-layer thickness test.

Because there are 12 equations to be solved for the RSE turbulence model, the CPU time is substantial. The computation for the completely doubled size mesh in every direction would be very time-consuming. Each mesh refinement is therefore implemented one at a time in each coordinate direction. Table 3 shows the mesh size for each refinement test. The following describes each test:

1) Refinement test in the x direction: This test halves the mesh spacing in the streamwise direction while the mesh sizes in the other directions are kept the same. This test will show whether the baseline streamwise mesh resolution is adequate to capture the boundary-layer development.

2) Refinement test in the y direction: This test halves the mesh spacing in the y direction. The y_1^+ at the channel entrance is reduced from the baseline case value $y_1^+ = 29$ to 20.9. This test will show whether the solution is sensitive to the different y_1^+ values used.

3) Refinement test in the z direction: This test halves the mesh spacing in the spanwise direction. The refinements in the y and z directions will show the influence of the resolution of the shock waves and vortices on the computational results.

4) Different upstream boundary-layer profile: As mentioned in the baseline case, it is difficult to match all upstream experimental parameters simultaneously. Therefore, this test investigates the effect of the incoming boundary-layer profile. In this test case, the incoming boundary-layer displacement thickness was reduced 45% from the baseline case, which resulted in an increase in the upstream heat transfer coefficient of 10%. This test will show whether the variations in the incoming boundary-layer profiles significantly affect the solution.

5) Different isothermal wall-temperature test: In the experiment, the temperature on the bottom wall was not uniform. There were insufficient experimental data that can be used to specify the wall temperature for the computation. The isothermal wall temperature is therefore treated as constant in the computation. This is based on the hypothesis that the heat transfer coefficient is independent of the wall temperature when the isothermal wall temperature is close to the adiabatic wall temperature. This test is to verify this hypothesis by using a wall temperature that is different from the baseline case. The wall temperature is set to 270 K, which is 5 K higher than the baseline one.

Figure 10 displays representative results of the convergence tests for the surface pressure along the throat middle line. The grid refinement in the x, y, and z directions does not perceptively change the pressure distribution. Also, the grid refinement changes the pressure distribution at x = 49, 79, and 112 mm (not shown) by less than 1%.

The computed surface pressure is insensitive to the upstream profile. The 45% reduction in the upstream displacement thickness causes a 7% change in the maximum surface pressure on the throat middle line. Also, the change in the isothermal wall temperature has a negligible effect on the surface pressure.

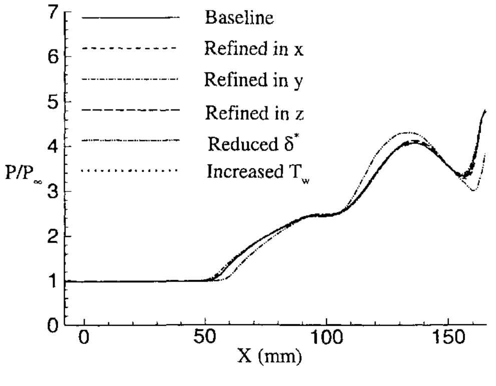

Fig. 10 Pressure distribution along the throat middle line at the bottom wall.

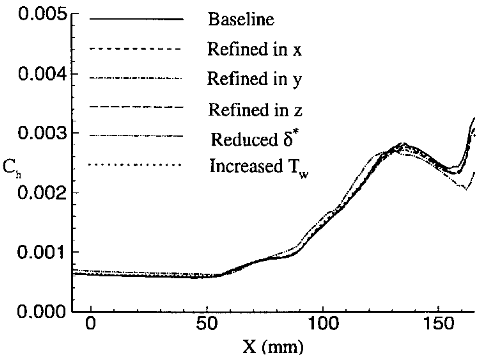

Fig. 11 Heat transfer coefficient distribution along the throat middle line.

Figure 11 displays representative results of the convergence tests for the heat transfer coefficient along the throat middle line. The maximum change in C_h is 4% for all convergence studies, which is less than the experimental uncertainty of ±10–15%. In particular, note that C_h is insensitive to the location y_1 at which the wall-function boundary conditions are applied, and to the incoming boundary-layer displacement thickness δ^*. Also, the C_h distribution changes by less than 2.5% at $x = 46$, 79, and 112 mm. Moreover, the computed T_{aw} changes by less than 1.5% for all convergence studies on the throat middle line and at $x = 46$, 79, and 112 mm.

V. Conclusions

The three-dimensional shock wave/turbulent-boundary-layer interaction caused by an asymmetric 7 × 11-deg double fin was calculated using the Reynolds-averaged Navier–Stokes equations with a full RSE model. An implicit approximate factorization method is employed for the temporal integration. Roe's scheme is used for evaluation of the convective terms with a third-order MUSCL-type differencing. A minmod total-variation-diminishing limiter is used and is essential for capturing the irregular turbulent–nonturbulent interface to make the computation stable. The computed surface pressure is in good agreement with the experiment. The computed heat transfer coefficient achieved 20% improvement compared with the results from the k–ϵ model with Chien's low-Reynolds-number correction. However, the maximum heat transfer coefficient still exceeded the experimental values by 80%. The computation resolved the counter-rotating vortex pair generated by the cross shock wave/turbulent-boundary-layer interaction, and predicted an enhanced turbulence intensity between the vortices. Mesh refinements indicate that the solution is grid converged on the basis of mesh size. Wall functions are used as boundary conditions to treat the solid walls. Within a proper range of y_1^+, the flow solutions are basically insensitive to the location of y_1^+. The test with reduced incoming boundary-layer thickness indicates that the heat transfer coefficient is generally not sensitive to the Reynolds number. The test with different isothermal wall temperature shows that the computed heat transfer is independent of the isothermal wall temperature when it is close to the adiabatic wall temperature. The computer code with the RSE turbulence model is quite robust.

Acknowledgments

This research was sponsored by U.S. Air Force Office of Scientific Research Grant F49620-93-1-0005 monitored by Len Sakell and Advanced Research Project Agency Contract DABT-63-93-C-0064 monitored by Bob Lucas (Hypercomputing and Design Project). The authors acknowledge the beneficial collaboration with Alexander Zheltovodov and his colleagues at the Institute of Theoretical and Applied Mechanics, Russian Academy of Sciences, Novosibirsk, Russia. The authors appreciate the helpful discussion with Joseph Morrison at Analytical Services and Materials, Inc. The authors would also like to thank Marianna Gnedin for her help in generating the upstream turbulent boundary-layer profiles using the boundary-layer code and Ken Tsang and Patrick McPartland for their work in visualizing the computed flowfield. The computations were performed at the Department of Defense Shared Resource Center: Naval Oceanographic Office at Stennis Space Center and at the Department of Defense High Performance Computing Center U.S. Army Engineers Waterways Experiment Station. Postprocessing was performed at the Rutgers University Supercomputer Remote Access Center.

References

[1] Knight, D., "Numerical Simulation of 3-D Shock Wave Turbulent Boundary Layer Interactions," *Special Course on Shock-Wave/Boundary Layer Interactions in Supersonic and Hypersonic Flows*, edited by G. Degrez, AGARD Rept. 792, 1993, pp. 3-1–3-32.

[2] Leschziner, M. A., "Computation of Aerodynamic Flows with Turbulence-Transport Model Based on Second-Moment Closure," *International Journal of Computer and Fluids*, Vol. 24, No. 4, 1995, pp. 377–392.

[3] Ladeinde, F., "Supersonic Flux-Split Procedure for Second Moments of Turbulence," *AIAA Journal*, Vol. 33, No. 7, 1995, pp. 1185–1195.

[4] Vandromme, D., and Minh, H. H., "About the Coupling of Turbulence Closure Models with Averaged Navier–Stokes Equations," *Journal of Computational Physics*, Vol. 65, Aug. 1986, pp. 386–409.

[5] Morrison, J. H., Gatski, T. B., Sommer, T. P., Zhang, H. S., and So, R., "Evaluation of a Near-Wall Turbulent Closure in Predicting Compressible Ramp Flows," *Near Wall Turbulent Flows*, edited by R. M. C. So, C. G. Speziale, and B. E. Launder, Elsevier, Amsterdam, 1993, pp. 239–250.

[6] Abid, R., Gatski, T. B., and Morrison, J. H., "Assessment of Pressure-Strain Models in Predicting Compressible, Turbulent Ramp Flows," *AIAA Journal*, Vol. 33, No. 1, 1995, pp. 156–159.

[7] Edward, C., "A Forebody Design Technique for Highly Integrated Bottom-Mounted Scramjets with Application to a Hypersonic Research Airplane," NASA TN D-8369, Dec. 1976.

[8] Sakell, L., Knight, D., and Zheltovodov, A., *Proceedings of the AFOSR Workshop on Fluid Dynamics of High Speed Inlets*, Dept. of Mechanical and Aerospace Engineering, Rutgers Univ., Piscataway, NJ, 1994.

[9] Gaitonde, D., Shang, J., and Visbal, M., "Structure of a Double-Fin Turbulent Interaction at High Speed," *AIAA Journal*, Vol. 33, No. 2, 1995, pp. 193–200.

[10] Narayanswami, N., Horstman, C. C., and Knight, D., "Computation of Crossing Shock Turbulent Boundary Layer Interaction at Mach 8.3," *AIAA Journal*, Vol. 31, No. 8, 1993, pp. 1369–1376.

[11] Narayanswami, N., Knight, D., Bogdonoff, S., and Horstman, C. C., "Interaction Between Crossing Oblique Shocks and a Turbulent Boundary Layer," *AIAA Journal*, Vol. 30, No. 8, 1992, pp. 1945–1952.

[12] Narayanswami, N., Knight, D., and Horstman, C. C., "Investigation of a Hypersonic Crossing Shock Wave/Turbulent Boundary Layer Interaction," *Shock Waves*, Vol. 3, No. 1, 1993, pp. 35–48.

[13] Garrison, T., Settles, G., Narayanswami, N., and Knight, D., "Structure of Crossing-Shock Wave/Turbulent Boundary Layer Interaction," AIAA Paper 92-3670, 1992.

[14] Garrison, T., and Settles, G., "Interaction Strength and Model Geometry Effects on the Structure of Crossing-Shock Wave/Turbulent Boundary Layer Interaction," AIAA Paper 93-0780, 1993.

[15] Garrison, T., Settles, G., Narayanswami, N., and Knight, D., "Comparison of Flowfield Surveys and Computation of a Crossing-Shock Wave/Turbulent Boundary Layer Interaction," AIAA Paper 94-2273, 1994.

[16] Bardina, J. E., and Coakley, T. J., "The Structure of Intersecting Shock Waves/Turbulent Boundary Layer Interaction Flow," AIAA Paper 95-2215, 1995.

[17] Bardina, J. E., and Coakley, T. J., "Three Dimensional Navier–Stokes Simulations with Two Equation Turbulence Models of Intersecting Shock Waves/Turbulent Boundary Layer at Mach 8.3," AIAA Paper 94-1905, 1994.

[18] Garrison, T., "The Interaction Between Crossing-Shock Waves and a Turbulent Boundary Layer," Ph.D. Thesis, Dept. of Mechanical Engineering, Pennsylvania State Univ., University Park, PA, 1994.

[19] Zheltovodov, A., Maksimov, A., Shevchenko, A., Vorontsov, A., and Knight, D., "Experimental Study and Computational Comparison of Crossing-Shock Wave-Turbulent Boundary Layer Interaction," *Proceedings of the International Conference on Method of Aerophysical Research—Part 1*, Russian Siberian Div., Academy of Sciences, 1994, pp. 221–230.

[20] Knight, D., Garrison, T., Settles, G., Zheltovodov, A., Maksimov, A., Shevchenko, A., and Vorontsov, S., "Asymmetric Crossing Shock Wave–Turbulent Boundary Layer Interaction," *AIAA Journal*, Vol. 33, No. 12, 1995, pp. 2241–2249.

[21] Gnedin, M., and Knight, D., "A Reynolds Stress Equation Turbulence Model for Compressible Flows, Part I: Flat Plate Boundary Layers," AIAA Paper 95-0860, 1995.

[22] Launder, B., Reece, G., and Rodi, W., "Progress in the Development of a Reynolds Stress Turbulence Closure," *Journal of Fluid Mechanics*, Vol. 68, April 1975, pp. 537–566.

[23] Rotta, J., "Recent Attempts to Develop a Generally Applicable Calculation Method for Turbulence Shear Flows," AGARD CP-93, 1971, pp. A1–A11.

[24] Sarkar, S., Erlebacher, G., Hussaini, M., and Kreiss, H., "The Analysis and Modelling of Dilatational Terms in Compressible Turbulence," *Journal of Fluid Mechanics*, Vol. 227, June 1991, pp. 473–493.

[25] Zeman, O., "Dilatational Dissipation: The Concept and Application in Modelling Compressible Mixing Layers," *Physics of Fluids*, Vol. 2, No. 2, 1990, pp. 178–188.

[26] Huang, P., Coleman, G. N., and Bradshaw, P., "Compressible Turbulent Channel Flow—A Close Look Using DNS Data," AIAA Paper 95-0584, 1995.

[27] Jones, W., and Launder, B., "The Prediction of Laminarization with a Two-Equation Model of Turbulence," *International Journal of Heat and Mass Transfer*, Vol. 15, Feb. 1972, pp. 301–304.

[28] Gnedin, M., and Knight, D., "Compressible Turbulence Wall Layer Reynolds Stress Equation Model Version No. 4," Internal Rept. 17, Dept. of Mechanical and Aerospace Engineering, Rutgers Univ., Piscataway, NJ, 1993.

[29] Wilcox, D., *Turbulence Modelling for CFD*, DCW Industries, Inc., 1993, La Cañada, CA, pp. 126–128, 279–286.

[30] Anderson, W., Thomas, J., and Van Leer, B., "Comparison of Finite Volume Flux Vector Splittings for the Euler Equations," *AIAA Journal*, Vol. 24, No. 9, 1986, pp. 1453–1460.

[31] Saffman, P., "A Model for Inhomogeneous Turbulent Flow," *Proceedings of the Royal Society of London*, Vol. A317, 1970, pp. 417–433.

[32] Roe, P., "Some Contributions to the Modelling of Discontinuous Flows," *Lectures in Applied Mathematics*, Vol. 22, Pt. 2, 1985, pp. 163–193.

[33] Hirsch, C., *Numerical Computation of Internal and External Flows*, Vol. 2, Wiley, New York, 1990, pp. 493–583.

[34] Zha, G.-C., and Knight, D., "Supersonic Turbulent Flat Plate Flow Calculation by Solving 3D Navier–Stokes Equations with a Reynolds Stress Equation Turbulence Model," TR 22, Dept. of Mechanical and Aerospace Engineering, Rutgers Univ., Piscataway, NJ, Dec. 1994.

[35] Zha, G.-C., and Knight, D., "Supersonic Flat Plate Flow Tests for 3D RSE Code," TR 21, Dept. of Mechanical and Aerospace Engineering, Rutgers Univ., Piscataway, NJ, June 1994.

[36] Knight D., Badekas, D., Horstman, C., and Settles, G., "Quasiconical Flowfield Structure of the Three-Dimensional Single Fin Interaction," *AIAA Journal*, Vol. 30, No. 12, 1992, pp. 2809–2816.

[37] Knight, D., "Determination of Constants in Reynolds Stress Equation Model," TR 6, Dept. of Mechanical and Aerospace Engineering, Rutgers Univ., Piscataway, NJ, Feb. 1993.

[38] Fernando, E., and Smits, A., "A Supersonic Turbulent Boundary Layer in an Adverse Pressure Gradient," *Journal of Fluid Mechanics*, Vol. 211, Feb. 1990, pp. 285–307.

[39] Zha, G.-C., and Knight, D., "Computation of 3D Asymmetric Crossing Shock Wave/Turbulent Boundary Layer Interaction Using a Full Reynolds Stress Equation Turbulence Model," AIAA Paper 96-0040, 1996.

[40] Chien, K. Y., "Predictions of Channel and Boundary Layer Flows with a Low Reynolds Number Turbulence Model," *AIAA Journal*, Vol. 20, No. 1, 1982, pp. 33–38.

Color reproduction courtesy of the U.S. Air Force Office of Scientific Research